STRUCTURAL BIOLOGY

Structures of closed and open conformations of dimeric human ATM

Domagoj Baretić,[1]* Hannah K. Pollard,[2] David I. Fisher,[2] Christopher M. Johnson,[1] Balaji Santhanam,[1] Caroline M. Truman,[2] Tomas Kouba,[1] Alan R. Fersht,[1] Christopher Phillips,[2] Roger L. Williams[1]*

ATM (ataxia-telangiectasia mutated) is a phosphatidylinositol 3-kinase–related protein kinase (PIKK) best known for its role in DNA damage response. ATM also functions in oxidative stress response, insulin signaling, and neurogenesis. Our electron cryomicroscopy (cryo-EM) suggests that human ATM is in a dynamic equilibrium between closed and open dimers. In the closed state, the PIKK regulatory domain blocks the peptide substrate–binding site, suggesting that this conformation may represent an inactive or basally active enzyme. The active site is held in this closed conformation by interaction with a long helical hairpin in the TRD3 (tetratricopeptide repeats domain 3) domain of the symmetry-related molecule. The open dimer has two protomers with only a limited contact interface, and it lacks the intermolecular interactions that block the peptide-binding site in the closed dimer. This suggests that the open conformation may be more active. The ATM structure shows the detailed topology of the regulator-interacting N-terminal helical solenoid. The ATM conformational dynamics shown by the structures represent an important step in understanding the enzyme regulation.

INTRODUCTION

ATM (ataxia-telangiectasia mutated) is a key regulator of the DNA damage response with a broad role in stress response cellular homeostasis. Double-strand DNA breaks in conjunction with the damage-sensing Mre11, Rad50, and Nbs1 (MRN) complex activate ATM, which phosphorylates hundreds of targets (*1*, *2*). ATM mutations are associated with the pleiotropic neurodegeneration disease ataxia telangiectasia (A-T), whose symptoms include malignancy and genome instability (*3*, *4*). ATM mutations are often accompanied by immunodeficiencies, premature aging, insulin resistance, and sterility (*5*, *6*). ATM is also activated by oxidation in an MRN-independent manner (*7*). ATM directly binds DNA (*8*, *9*), but the MRN complex facilitates its recruitment to sites of DNA damage (*10*).

ATM is a member of the phosphatidylinositol 3-kinase–related protein kinase (PIKK) family that also includes protein kinases mTOR (mechanistic target of rapamycin) and DNA-PKcs (DNA-dependent protein kinase catalytic subunit) (*1*, *11*, *12*). The C-terminal PIKK-conserved unit, which we refer to as the FATKIN, consists of a unique region known as the FAT [FRAP (FKBP12-rapamycin–associated protein), ATM, and TRRAP (transformation/transcription domain-associated protein)] and a C-terminal phosphatidylinositol 3-kinase–like kinase domain (here abbreviated as KIN) but makes up no more than one-half of any PIKK. All PIKKs have about 1400 to 3000 residues at their N termini consisting predominately of helical repeats known as HEAT (huntingtin, elongation factor 3, protein phosphatase 2A, and TOR1) repeats, which we will refer to as the N-solenoid.

Several reconstructions of yeast and human ATM at resolutions from 14 to 30 Å have been reported using electron microscopy (*9*, *13*, *14*). Most recently, an 8.7 Å resolution electron cryomicroscopy (cryo-EM) single-particle reconstruction was reported for the *Schizosaccharomyces pombe* Tel1 (*15*), where it was not possible to trace the course of the polypeptide. To gain insight into the structural basis for ATM activation, we have determined cryo-EM structures of human ATM at a highest resolution of 4.4 Å.

[1]Medical Research Council Laboratory of Molecular Biology, Cambridge CB2 0QH, UK. [2]Discovery Sciences, Innovative Medicines and Early Development Biotech Unit, AstraZeneca, Darwin Building, Cambridge CB4 0WG, UK.
*Corresponding author. Email: rlw@mrc-lmb.cam.ac.uk (R.L.W.); domi@mrc-lmb.cam.ac.uk (D.B.)

RESULTS

Our cryo-EM analysis and multiangle light scattering (MALS) and biochemical assays indicate that purified human ATM is a dimer and is enzymatically active (Fig. 1A, figs. S1 to S5, and table S1). Subclassification of ATM particles indicated the presence of five three-dimensional (3D) classes. We have structurally interpreted four of these, classes A to D (fig. S5). Two types of dimers are present in the sample. One type of dimer has symmetrically related FATKINs (Fig. 1B), and we will refer to these as "closed" dimers (fig. S5, classes A and B). A second type of dimer is asymmetric (Fig. 1C), and we will call these "open" dimers (fig. S5, classes C and D). Our structures suggest that the open dimer might be a more active form of ATM.

Structure of the closed ATM dimer

The 3D class A (fig. S5) constitutes the closed dimer in which density is visible for both protomers. The closed dimer has a butterfly shape (Fig. 1B), where the N-solenoids form the wings and the FATKINs constitute the head. The path of the polypeptide in the closed dimer is clear, which allowed us to build an atomic model for the entire molecule into a density with an overall resolution of 4.7 Å (Fig. 1B, figs. S6 to S8, and table S2). In this model, we have not included side-chain atoms beyond Cβ because side-chain density was only rarely evident at this resolution. The N-solenoid has an N-terminal Spiral followed by a second region that we divide into the N-pillar, Bridge, C-pillar, Railing, and Cap (Figs. 1, B and E, and 2A). This second region was noted as the "C-Pincer" in the structurally unresolved density of the yeast Tel1 (*15*). The Pincer is then followed by the FATKIN.

The local resolution is highest in the C-terminal half of ATM (Pincer-FATKIN), which was reconstructed to a resolution of 4.4 Å (Fig. 1B and fig. S5). At this resolution, most helices appear as spirals (fig. S9), and the loops connecting secondary structure elements are mainly ordered. The ATM FATKIN can be divided into five domains: tetratricopeptide repeat domains TRD1 (α0 to α3, residues 1903 to 2025), TRD2 (α4 to α12, residues 2032 to 2190), and TRD3 (α13 to α22, residues 2195 to 2476); HRD (HEAT-repeats domain) (α23 to α28, residues 2484 to 2612); and a kinase domain (residues 2618 to 3056) (figs. S10 and S11). These regions assemble into a structure that is broadly

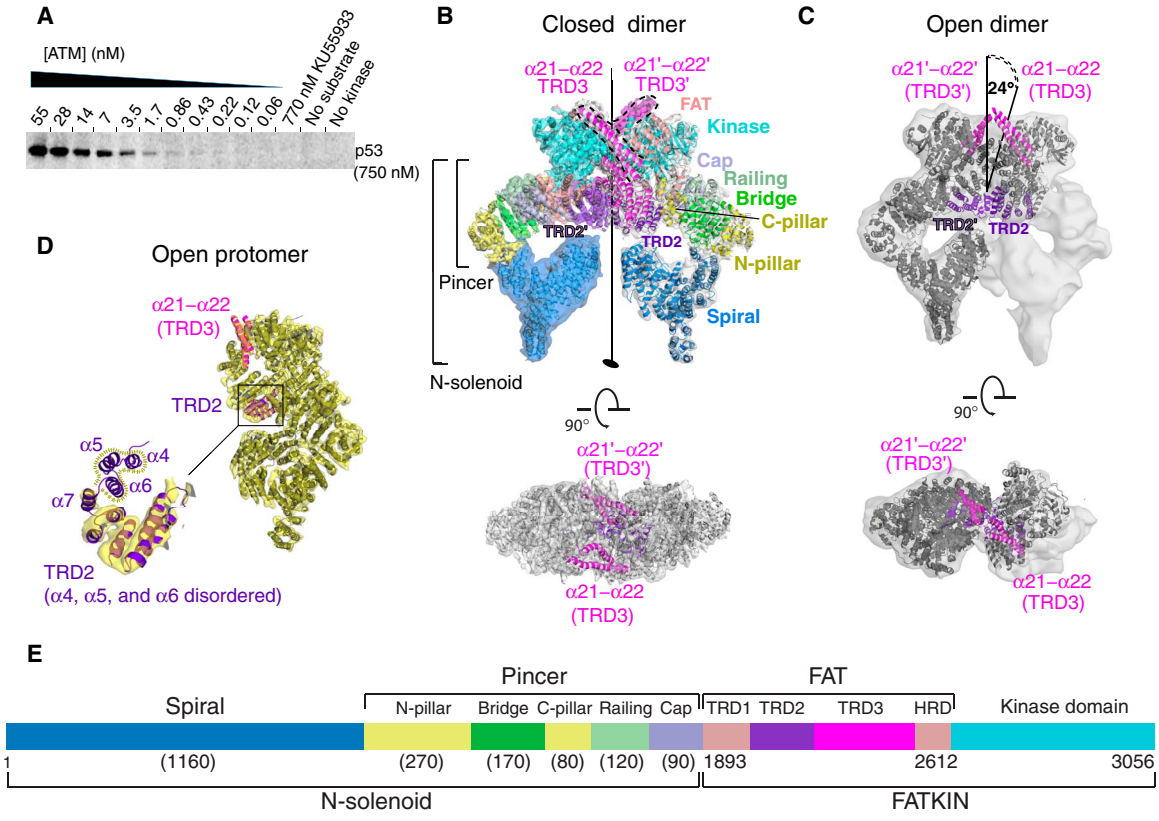

Fig. 1. Structures and activity of human ATM dimers. (**A**) Basal catalytic activity of purified human ATM with full-length p53 substrate (visualized by ^{33}P autoradiography). (**B**) Side and top views of the closed dimer are shown as ribbon diagrams colored by domains within EM densities at a resolution of 4.4 Å for the Pincer-FATKIN and 5.7 Å for the N-terminal Spiral. The twofold symmetry axis is shown as a black line. (**C**) Side and top views of the open dimer having two protomers at a resolution of 11.5 Å (fig. S5, 3D class C). One protomer and a second FATKIN were fit into the density. The right molecule in the open dimer is tilted about 24° with respect to the orientation it would have in the closed dimer. (**D**) The open protomer (from 3D classes C and D) model and the map at an overall resolution of 5.7 Å (the Pincer-FATKIN region at a resolution of 4.8 Å). The inset shows details of the TRD2 region, where much of it is disordered in the open protomer. Helices α4, α5, and α6 are not ordered in the open protomer, but for reference, they are shown in the inset, surrounded by a dashed yellow curve. (**E**) A bar diagram of human ATM (approximate numbers of residues in the N-solenoid domains are shown in parentheses).

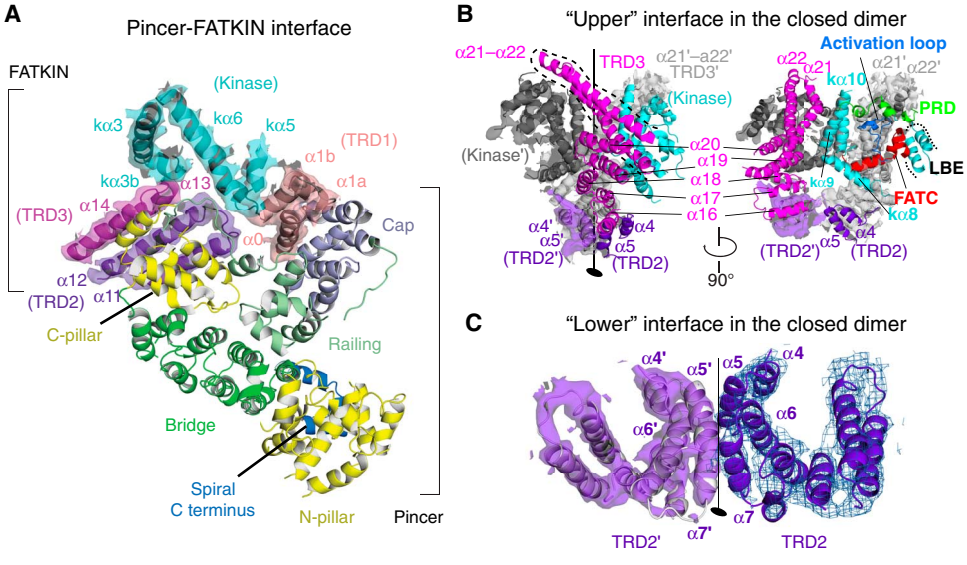

Fig. 2. Views of the Pincer-FATKIN interface and the dimer interface. (**A**) A closeup view of the Pincer domains and their interactions with the FATKIN. (**B**) The bipartite interface between the two protomers in the closed dimer. The upper interface includes portions of the kinase domain and TRD3. (**C**) The lower interface, primarily including TRD2 and a portion of TRD3, shown as ribbons with the density of the closed dimer interface (purple and blue).

similar to the structure of the mTOR FATKIN (fig. S10) (*16*); however, the ATM FATKIN mediates ATM dimerization, and this is important for the ATM activation mechanism.

The interface in the closed dimer

The closed dimer interface can be divided into the "upper" and the "lower" interface (Fig. 2, B and C). The upper interface involves TRD3 in one molecule forming compelling interactions with the kinase domain of its dimeric partner. The lower interface involves TRD2 from one molecule interacting with TRD2 and TRD3 of the other molecule.

Several kinase domain C-lobe elements are important for the transition between closed and open dimers. The FAT C-terminal (FATC), LST8-binding element (LBE), activation loop, and PIKK regulatory domain (PRD; helices kα9b, kα9c, and kα9d) form a compact arrangement that we will refer to as the FLAP [FATC, LBE, activation loop, and PRD] (Fig. 3A), which is key to the regulation of ATM. Because the TRD3 helices α21 and α22 (residues 2378 to 2476) interact with all of the elements of the FLAP, we will refer to this helical hairpin as the FLAP-binding element (FLAP-BE). Much of the upper interface consists of this FLAP/FLAP-BE interaction (Fig. 2B). The FLAP-BE of one molecule pushes on helices kα9c and kα9d (residues 2966 to 2979) in the PRD of the other molecule, causing kα9c and kα9d to enter the active site (Fig. 3A and fig. S12). We modeled a peptide substrate bound to ATM based on the structure of CDK bound to its substrate (Fig. 3A). In this model, a peptide substrate would completely clash with the helices kα9c/kα9d and FLAP-BE, suggesting that the closed dimer might be less active, because the peptide substrate would have to compete with the PRD for binding to the active site (movie S1).

Structure of the N-terminal solenoid

The N-solenoid has six domains (Fig. 1, B and E, and fig. S13). The ATM Spiral (residues 1 to 1161) has roles in binding substrates, regulators, and adaptors. Two corkscrew-like turns of the Spiral wrap around a 30 Å open cavity (figs. S13A and S14C). The first turn of the Spiral contacts the second turn where several short helices, which may be part of an extension from the N-pillar, are visible and may function to rigidify the Spiral (fig. S14).

The exposed N-terminal tip of the Spiral bears the Tel1/ATM N-terminal (TAN) motif (residues 18 to 40) (Fig. 4A) (*17*), which is essential for the ATM function in yeast. Spiral residues 90 to 97 interact with some ATM substrates, including p53, BRCA1, and LKB1 (Fig. 4A) (*18*). The binding site for Nbs1 of the MRN complex (*19*) maps approximately to the Spiral/N-pillar interface (Fig. 4A). ATM phosphorylates p53 in response to DNA damage (*20*), but p53 binding was only detected after ATM activation by DNA damage, which led to the proposal that this N-terminal region becomes exposed in a dimer-to-monomer transition (*18*). The structure shows that the p53-binding region is not involved in the dimer interface (Fig. 4A) and is exposed in all states that we observe. It may be that, in cells, an ATM binding partner could stabilize the closed dimer by binding to this site. If this blocking partner were removed in the activation process, it would explain the current observations. Similarly, activating partners such as Nbs1 or ATMIN (*19*, *21*) might bind to this N-terminal region to lock the enzyme in the open conformation.

The ATM and TOR N-solenoids share four structural modules: the Spiral, Bridge, Railing, and Cap (fig. S15); however, these elements are arranged differently in space (fig. S16). The two pillars (Fig. 2A) are ATM N-solenoid modules absent in TOR. The N-terminal end of the Spiral in TOR/mTOR is freely accessible (*22*, *23*), thereby correcting an earlier proposed topology that traced this region in the reverse direction (*24*). This corrected topology is consistent with the topology recently reported for DNA-PKcs (*25*) and the topology we observe for the ATM Spiral.

Structure of the ATM FAT domain

The FAT domain of ATM wraps around the kinase domain (fig. S10A). We have mapped three PIKK-specific polar interactions between the FAT and the kinase domains (*16*) onto the ATM FATKIN: Glu^{1959}-Arg^{2849}, Arg^{2486}-Glu^{2950}, and Gln^{2522}-Gln^{2730}. These residues are highly conserved in ATMs (fig. S11). Mutation R2849P at this interface is associated with A-T disease (*26*), whereas an R2486P mutation is associated with T cell prolymphocytic leukemia (*27*), suggesting that these interactions are important to stabilize ATM.

Ser^{1981} in a loop between α1c/α2 helices of TRD1 (Fig. 4A) is a site of autophosphorylation and is part of a metazoan-specific insertion in ATM (*15*). In vitro, the S1981A mutation has no effect on kinase activity (*2*). However, in cells, Ser^{1981} phosphorylation enables ATM to remain associated with sites of double-strand DNA breaks by binding to the MDC1 FHA domain (*28*). The Ser^{1981} loop is not ordered in either the open or closed dimers, so it is unlikely that it controls the intrinsic activation state of the enzyme.

Structure of the open ATM dimer

We observed one class of the open dimer (asymmetric) in which both full protomers are visible (fig. S5, 3D class C). We have refined this class as the open dimer at a resolution of 11.5 Å (fig. S5). There is a second class of open dimers in which only one protomer is fully visible, which we will refer to as the open multi-conformer dimer (fig. S5, 3D class D). The full protomer in this class is associated with a second protomer that has only weak density for the Pincer-FATKIN and no density for the Spiral. The weak density probably arises from the protomer being averaged in an ensemble of orientations/conformations, as the dimer transitions between closed and open states (Fig. 4B and fig. S5). Because both classes C and D have one full protomer, we combined these and carried out masked refinement to obtain the structures of the open protomer at a resolution of 5.7 Å and its Pincer-FATKIN region at a resolution of 4.8 Å (Fig. 1D and fig. S5).

In the 11.5 Å resolution density for the open dimer with two full protomers (3D class C), we could readily fit the model for the open protomer (see above) and a second FATKIN molecule (Fig. 1C and fig. S5). There is a ratcheted rotation of about 24° for one FATKIN with respect to the other, compared with the FATKINs in the closed dimer (Fig. 1, B and C).

In the closed conformation, the FLAP/FLAP-BE interaction restricts access to the ATM substrate–binding site (Fig. 3A). However, the open dimer does not make the full set of contacts observed in the closed dimer. Notably, there is no intermolecular contact between the FLAP and the TRD3 in the upper interface of the open dimer (Figs. 1C and 3B and fig. S12). Moreover, PRD helices kα9d and most of kα9c are disordered, leaving sufficient space for a peptide substrate to bind (Fig. 3B). Release of constraints on the PRD in the open dimer arises from loss of contacts between the FLAP and the dimer-related FLAP-BE.

In the lower interface of the open dimer, density for only part of TRD2 is visible (Fig. 1D). However, contacts with α7 of TRD2 and α16 and α18 of TRD3 are still present (fig. S17). Therefore, in the open dimer, only the lower interface is partially retained with no preserved contacts in the upper interface.

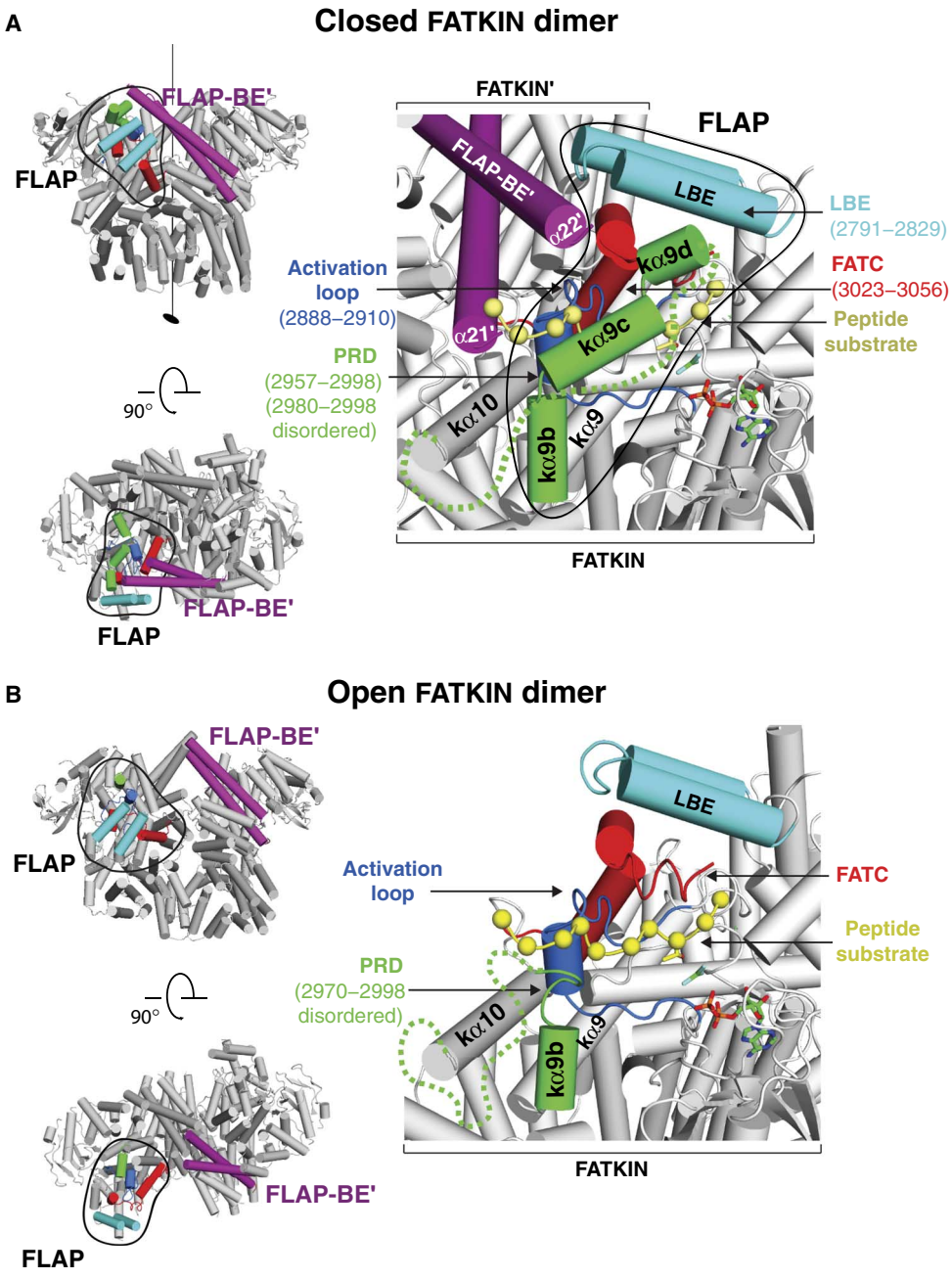

Fig. 3. Open and closed ATM dimer conformations of the active site. (**A**) The side view on the left shows the FATKIN arrangement in the closed dimer. The FLAP-BE′ (purple) from the symmetry-related molecule restricts the PRD to a conformation that blocks the substrate peptide from entering the active site (right panel). The location of ADP-F_3Mg was modeled on the basis of the crystal structure of the mTOR FATKIN [Protein Data Bank (PDB) ID 4JSV]. The location of the substrate peptide (yellow spheres) was modeled by superimposing a peptide-bound Cdk2 [PDB ID 3QHW (*50*)] onto the ATM active site. (**B**) A model of the active site of the 4.8 Å resolution open protomer (right panel). The side view on the left is the arrangement of the two FATKIN moieties in the 11.5 Å resolution open dimer. The green dashed lines in each panel represent the disordered portion of the PRD.

DISCUSSION

Our structural work shows that ATM can form an open dimer with a limited intermolecular interface and a tightly packed closed dimer with a larger interface. The active site of the open dimer is compatible with substrate binding, whereas the PRD acts as a pseudosubstrate to block the active site in the closed dimer. This provides structural insight into several previous observations regarding the PRD. The PRD was named on the basis of findings that mutations in this region prevent ATR activation and that the analogous region in DNA-PKcs is important for its regulation (*29*). An earlier study showed that partial deletion of the PRD in mTOR led to a hyperactive enzyme (*30*). The shift of the PRD between the closed and the open dimers suggests

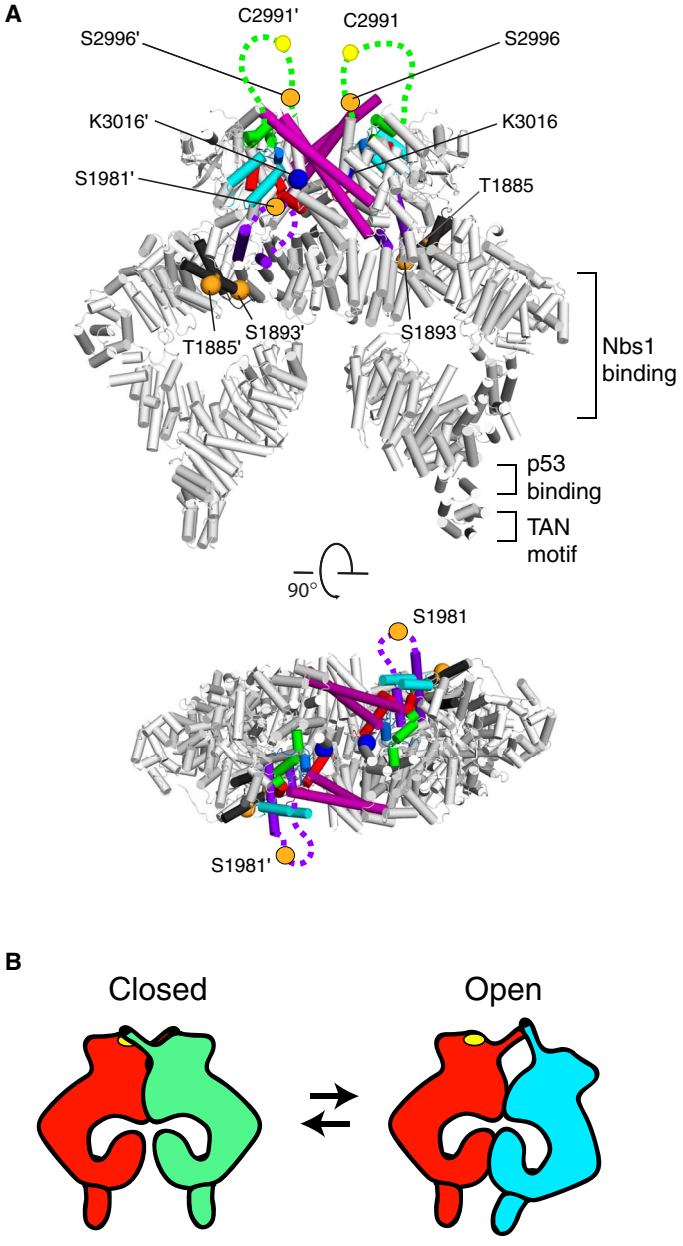

Fig. 4. A dynamic equilibrium of ATM dimers may be regulated by interactions with activators and substrates. (**A**) A model of ATM highlighting known activating influences on ATM. The orange spheres denote locations of four sites of autophosphorylation (Ser^{1981} and Ser^{2996} are in disordered loops suggested by dashed lines). The FLAP-BE (purple), FATC (red), LBE (cyan), activation loop (light blue), and PRD (green) are highlighted. Cys^{2991}, whose oxidation is associated with ATM activation, is marked by a yellow sphere in the disordered PRD loop (suggested by a dashed line). The Lys^{3016} acetylation site in the dimeric contact of the FATC is shown as a blue sphere. The approximate locations of the N-terminal TAN motif and the Nbs1 and p53 binding sites are indicated. (**B**) A schematic representation of the ATM dynamic equilibrium between open and closed dimers. Specific substrates or regulators could differentially recognize variations in the dimer interface.

a more general mechanism for ATM regulation. Studies of oxidative ATM activation showed that Cys^{2991} is involved (*7*). Cys^{2991} is approximately in the middle of the PRD, in a disordered region (Fig. 4A). Consequently, the ATM structure does not enable us to make a definitive statement as to how an intermolecular Cys^{2991}–Cys^{2991} disulfide bond might activate the enzyme.

ATM is posttranslationally modified in a variety of different ways (Fig. 4A). In addition to the autophosphorylation of Ser^{1981}, which is widely used as a marker of ATM activation, ATM is also acetylated on Lys^{3016} just before the FATC domain upon DNA damage (*31*, *32*). The helix and the loop just preceding the FATC region form an elbow that could control the position of the FATC. The elbows from the two subunits in the closed dimer interact with each other at the twofold axis of the dimer. Lys^{3016} is sufficiently close to Glu^{3021} or Tyr^{2864} that their side chains may interact. Acetylation of Lys^{3016} could break these interactions, resulting in a conformational change of FATC that would help break the upper contacts in the dimer, thereby favoring an open dimer. This would be consistent with the observation that mutation of Lys^{3016} prevents dissociation of ATM dimers (*32*).

The open dimer has a different and less extensive intermolecular interface compared to the closed dimer, yet both closed and open states coexist, at least under the cryo-EM conditions. It is possible that these two states are in equilibrium in solution (Fig. 4B). An early work proposed that ATM is an inactive dimer and that DNA damage induces Ser^{1981} autophosphorylation, leading to dimer dissociation and activation (*2*). We find that the purified dimeric ATM used in this study is enzymatically active (Fig. 1A and fig. S2). Our cryo-EM structures show that about half of the particles are in an open conformation (fig. S5). It is possible that these open dimers account for the activity of the recombinant protein that we see in solution; however, we have no direct way to demonstrate what the active conformation in solution is. Although we see no evidence for free monomers, it may be possible for ATM monomers to form under some conditions. The open dimer that has a more limited intermolecular interface than the closed dimer may be more readily dissociated by binding other partners such as the MRN and DNA (*10*) or by harsher ATM purification protocols that include high salt concentration (*10*). It is also possible that the presence of substrate would affect the oligomeric state of the enzyme. Our structures represent a framework that will help guide future work aimed at understanding regulation of ATM in both DNA damage response and other contexts.

MATERIALS AND METHODS

Recombinant human ATM expression

Full-length ATM (residues 1 to 3056, Q13315) with an N-terminal FLAG tag (MDYKDDDDKH) was synthesized and codon-optimized for expression in mammalian cells. The FLAG-ATM gene was cloned into pDEST12.2-OriP to generate pDEST12.2-OriP–ATM, as described previously (*33*). All DNA solutions used for transfection were prepared under sterile conditions at 1 mg/ml in TE buffer [10 mM tris-HCl and 1 mM EDTA (pH 7.4)].

Small-scale transfections were carried out in Expi293F (Thermo Fisher Scientific, catalog no. A14528) and CHO (Chinese hamster ovary)–EBNA (Epstein-Barr virus nuclear antigen)–GS (glutamine synthase) cells (*34*) to determine the highest-yielding system (data not shown). For protein supply, Expi293F cells were transfected on a 1-liter scale. A 450-ml culture was seeded at 2×10^6 cells/ml 24 hours before transfection. To generate the transfection complexes, 3 mg of 40-kDa polyethylenimine hydrochloride (Polysciences, catalog no. 24765) was mixed with 750 μg of pDEST12.2-OriP–ATM in a total volume of 50-ml Expi293 Expression Medium (Thermo Fisher Scientific, catalog no. A1435101) and incubated for 15 min at room temperature. After

incubation, the transfection complexes were added to the culture. The cells were incubated at 37°C, 5% CO_2, and 140 rpm in an orbital incubator (25-mm orbit). At 24 hours after transfection, the culture was diluted with 500 ml of Expi293F Expression Medium. At 4 days after transfection, cells were harvested by centrifugation at 10,000*g* for 20 min.

Human ATM purification for cryo-EM

The cell pellet from 1 liter of culture was resuspended in 100 ml of cold lysis buffer [50 mM Hepes (pH 7.5, 23°C), 150 mM NaCl, 100 mM arginine (Sigma-Aldrich, catalog no. A-5006), 10% (v/v) glycerol, two tablets of complete EDTA-free protease cocktail inhibitors (Roche) per 0.1 liter, and 1000 U of Pierce Universal Nuclease (Thermo Fisher Scientific, catalog no. 88702) per 0.1 liter]. The cells were further disrupted by sonication for 75 s (5× 15 s on/off) at 40% power (Vibra-Cell, Sonics and Materials Inc.) at 4°C. The whole cell lysate was cleared by centrifugation in a Ti45 rotor at 19,500*g* for 45 min. The following steps were performed in a cold room, and a roller was used for the incubation steps, unless mentioned otherwise. A 3-ml slurry of anti-FLAG resin (M2 agarose affinity gel; Sigma-Aldrich, catalog no. A2220) was first washed with water and then with buffer A [50 mM Hepes (pH 7.5, 23°C), 150 mM NaCl, 100 mM L-arginine, and 10% (v/v) glycerol]. The cleared lysate and the resin were mixed in a 250-ml conical bottle (Corning) and incubated for 2 hours. The resin was spun down in a Rotanta 460 swing-out rotor at 1900*g* for 2 min. The supernatant was removed by pipetting, and the resin was resuspended in buffer A before it was transferred to a 2.5 cm × 10 cm glass Econo-Column (Bio-Rad). The resin was then washed with 2× 50 ml of buffer A followed by a 2× 50-ml wash with buffer B [50 mM Hepes (pH 7.5, 23°C), 150 mM NaCl, 10% (v/v) glycerol, and 1 mM dithiothreitol (DTT)]. Elution buffer was prepared by diluting 3X FLAG peptide stock solution [peptide (5 mg/ml), 10 mM tris (pH 7.4, 23°C), and 150 mM NaCl] to the peptide (200 μg/ml) using buffer B. The resin was gently resuspended in 5 ml of the elution buffer and incubated for 10 min while sitting at 4°C. A total of 5× 5 ml of elution fractions were collected in this way. The combined elution fractions (25 ml) were transferred to dialysis tubing [SnakeSkin, 10,000 molecular weight cutoff (MWCO), Thermo Fisher Scientific] and dialyzed overnight in 5 liters of the dialysis buffer [50 mM Hepes (pH 7.5, 23°C), 150 mM NaCl, 0.01% (v/v) Tween 20, and 2 mM tris(2-carboxyethyl) phosphine (TCEP)]. The dialyzed protein was then concentrated (50,000 MWCO, Amicon Ultrafree concentrator) to 50 μl, spun for 1 min at 20,238*g* in a tabletop centrifuge to remove large aggregates, and finally purified by size exclusion chromatography (SEC) (at a flow rate of 250 μl/min, TSKgel G4000SWXL, Tosoh Corporation Bioscience) in 50 mM Hepes (pH 7.5, 23°C), 150 mM NaCl, 0.01% (v/v) Tween 20, and 2 mM TCEP. Purified protein was concentrated to 1.2 mg/ml (3.4 μM), plunge-frozen in liquid nitrogen in 10-μl aliquots, and stored at −80°C until it was used for the cryo-EM grid preparation.

Human ATM purification for kinase assay

The protein was purified by affinity chromatography as described above, with some minor modifications. Notably, after washing the resin with buffer A, a reducing buffer C [50 mM Hepes (pH 7.5, 23°C), 150 mM NaCl, 10% (v/v) glycerol, and 2 mM TCEP] was used for a second wash. Elution buffer was prepared by diluting 3X FLAG peptide stock solution to the peptide (100 μg/ml) using buffer C. The elution fractions were combined, and ATM was concentrated (50,000 MWCO, Amicon Ultrafree concentrator) to 1.5 μM. Protein was aliquoted, flash-frozen, and stored at −80°C until it was used for the kinase assay.

Human p53 expression and purification for kinase assay

A full-length variant of human p53 carrying four stabilizing mutations (M133L, V203A, N239Y, and N268D) (*35*, *36*) in the DNA binding domain was expressed as an N-terminal His_6-lipoyl domain fusion in *Escherichia coli* C41 (DE3) cells (Lucigen) and purified at 4°C by a combination of Ni–nitrilotriacetic acid, heparin affinity, and gel filtration chromatography, as described previously (*37*, *38*).

Briefly, expression cultures were incubated at 37°C and shaken at 250 rpm until an optical density at 600 nm of ~0.8 was reached. Zinc sulfate was added to a final concentration of 50 μM, and protein expression was induced with 500 μM isopropyl β-D-1-thiogalactopyranoside at 22°C. Cells were harvested 16 hours later by centrifugation and lysed using a high-pressure homogenizer (Avestin, Biopharma) in a lysis buffer containing 50 mM Hepes (pH 7.4, 4°C), 500 mM NaCl, 5% (v/v) glycerol, 20 mM imidazole, 0.05% (v/v) Tween 20, 8 mM β-mercaptoethanol, EDTA-free protease inhibitor cocktail (Roche), ribonuclease A (Sigma-Aldrich), deoxyribonuclease I (Sigma-Aldrich), and lysozyme (Sigma-Aldrich). Clarified lysate was loaded onto a HisTrap FF Crude column (GE Healthcare) and step-eluted with 50 mM Hepes (pH 7.4, 4°C), 500 mM NaCl, 5% (v/v) glycerol, 500 mM imidazole, and 8 mM β-mercaptoethanol. Fractions containing recombinant protein were pooled, and the N-terminal His_6-lipoyl domain was cleaved off by a tobacco etch virus protease (a Gly-Gly-Ser sequence remains to precede the initial Met of p53 full-length sequence in the final cleavage product). The protein was subsequently dialyzed for 20 hours against the dialysis buffer containing 20 mM Hepes (pH 7.4, 4°C), 150 mM NaCl, 200 mM arginine, 10% (v/v) glycerol, and 4 mM DTT and then loaded onto a HiTrap Heparin HP column (GE Healthcare) followed by column equilibration in the dialysis buffer containing 210 mM NaCl. The protein was then step-eluted with the dialysis buffer containing 450 mM NaCl. Finally, the elution fractions were directly subjected to SEC using an XK 26/70 Superose 6 prep grade column (GE Healthcare) equilibrated in 20 mM Hepes (pH 7.3, 4°C), 500 mM NaCl, 200 mM arginine, 10% (v/v) glycerol, and 4 mM DTT. The protein was eluted at 3 mg/ml (67 μM), and the aliquots were flash-frozen in liquid nitrogen for storage at −80°C before p53 was used for the kinase assay.

ATM kinase assay

The kinase assay was adapted from published protocols for ATM (*7*, *10*). The catalytic activity of human ATM (stored at −80°C and then thawed for the assay) prepared in the purification buffer C [25 mM Hepes (pH 7.5, 23°C), 150 mM NaCl, 10% (v/v) glycerol, and 2 mM TCEP] was determined using the full-length human p53 substrate at a concentration of 750 nM. The reactions were carried out in a final volume of 14 μl in two different reaction buffers prepared at room temperature (23°C): (i) the purification buffer [25 mM Hepes (pH 7.5, 23°C), 150 mM NaCl, 10% (v/v) glycerol, and 2 mM TCEP, supplemented with 5 mM $MgCl_2$] and (ii) the cryo-EM buffer [25 mM Hepes (pH 7.5, 23°C), 25 mM tris (pH 8.8, 23°C), 150 mM NaCl, 0.01% (v/v) Tween 20, and 2 mM TCEP, with the addition of 5 mM $MgCl_2$]. The ATM-specific inhibitor KU55933/AZ12622702 (AstraZeneca) was dissolved in dimethyl sulfoxide and then added to the reaction at a concentration of 770 nM. The reactions were started with the addition of 100 μM adenosine 5′-triphosphate (ATP) and 0.3 μCi [γ-^{33}P]ATP, following the incubation for 15 min at 30°C. The reactions were stopped with the addition of SDS–polyacrylamide gel electrophoresis (PAGE) loading buffer. An aliquot of 11 μl of each reaction mixture was resolved by SDS-PAGE using 4 to 12% NuPAGE bis-tris gel (Invitrogen, Thermo

Fisher Scientific). The gel was stained in Coomassie (InstantBlue, Expedion), destained in water, dried for 1 hour at 80°C (electrophoresis slab gel dryer), and exposed for up to 24 hours to a storage phosphor screen (GE Healthcare Molecular Dynamics). The ^{33}P incorporation was analyzed using a Typhoon FLA 7000 PhosphorImager. In addition, the p53 phosphorylation was detected by mass spectrometry analysis of the above catalytic reactions containing nonradioactive ATP.

Cryo-EM grid preparation and microscopy

Several freezing conditions were tested to obtain single particles of human ATM distributed in thin ice (we found that a thin carbon support gave rise to a strong preferential orientation of ATM). ATM was defrosted on ice and mixed with 1 volume of the cryo-EM freezing solution [50 mM tris (pH 8.8, 23°C), 150 mM NaCl, 0.01% (v/v) Tween 20, and 2 mM TCEP]. An aliquot of 3 µl (final protein concentration of ~0.6 mg/ml) was applied to a plasma-cleaned (NanoClean model 1070, vacuum of 10^{-5} mbar, argon/oxygen ratio of 9:1, 70% power, 0.331 cubic centimeter per minute flow, and 20-s exposure) grid with no support [QUANTIFOIL R1.2/1.3 Au (300 mesh) or UltrAuFoil R1.2/1.3 (300 mesh)] and then blotted for 12 s and plunge-frozen in liquid ethane using a custom-built manual plunger [Medical Research Council Laboratory of Molecular Biology (MRC LMB), Cambridge, UK] at 4°C. An FEI Titan Krios operated at 300 keV was used for data collection. The micrographs were recorded either manually or in a semiautomated fashion [University of California, San Francisco Image4 (*39*)]. We used a Gatan K2 Summit direct electron detector in a super-resolution counting mode at a calibrated magnification of 35,714× (nominal magnification of 97,902×), which resulted in a physical pixel size of 1.43 Å. A GIF Quantum Energy Filter with a slit width of 20 eV was used. A total exposure of about 42 $e^-/Å^2$ over 16 s (~2.6 $e^-/Å^2$ per second or ~5.3 e^- per pixel per second) was dose-fractionated in 20 movie frames. A defocusing range of −2.5 to −4 µm in 0.25-µm steps was applied during the data collection.

Cryo-EM image processing

We collected a total of 2720 good 20-frame movie stacks (see example in fig. S3) that were corrected for whole-image drift using the MotionCorr program (*40*). The graphics processing unit (GPU)–accelerated program Gctf (*41*) was used for determining the contrast transfer function parameters from the drift-corrected averaged images. The subsequent data processing steps were done in RELION 1.4 (*42*, *43*), if not specifically mentioned.

At first, about 2500 particles were manually picked with a particle mask of 260 Å in diameter, extracted with a 300 pixel × 300 pixel box size to generate initial reference-free 2D class averages. Reasonable 2D class averages were low-pass–filtered to 20 Å and used as a template for a reference-based particle autopicking (*44*) of the first data set containing 649 micrographs.

The automated particle selection was manually checked for each micrograph to remove obvious protein aggregates and contaminants to finally extract 67,756 particles. Further reference-free 2D classification gave class averages with prominent features altogether containing 21,135 particles (fig. S3B). An initial 3D model (fig. S4A) was reconstructed in EMAN2 (*45*) by imposing C2 symmetry and using nine 2D class averages. Projections of the initial model were in agreement with the experimentally obtained 2D class averages. A 3D classification restricted to five classes was performed without imposing symmetry (C1), using the 60 Å low-pass–filtered initial EMAN2 model, an angular sampling of 7.5°, and a regularization parameter T of 4, and without doing local angular searches around the refined orientations during 40 iterations. A single 3D class that matched well with the experimental 2D projections had clear C2 symmetry and the highest accuracy of rotations (1.98°) (fig. S4A), and this was used as a new initial 3D model for further reconstructions. A second round of the 3D classification (following the steps from above) using the new initial 3D model resulted in three prominent classes that indicated conformationally distinct species (fig. S4B). To increase the number of good particles, we combined the best three classes (a total of 16,873 particles) to obtain an interpretable cryo-EM map of human ATM. Auto-refinement of the combined classes resulted in a conformationally averaged reconstruction at an overall resolution of 7.5 Å (accuracy of the rotational alignment was 2.79°, and the translational alignment accuracy was 1.17 pixels) (fig. S4B). We used this cryo-EM map to determine the handedness by manually fitting in a model of the mTOR FATKIN (PDB ID 4JSP was manually modified by deleting the FRB domain, using Coot) (fig. S4B).

To select particles from the entire data set, we used the GPU-accelerated program Gautomatch [K. Zhang, MRC LMB (www.mrc-lmb.cam.ac.uk/kzhang/)]. The 2D classes obtained earlier were used as a new template for the automated particle selection. After refiltering the selected particle coordinates [using the script box_filter2rl.com (www.mrc-lmb.cam.ac.uk/kzhang/Gautomatch/)] and manually examining each micrograph, a total of 371,671 particles were subsequently cleared from bad particles during the two cycles of 2D classification. A total of 139,086 particles were included in further data processing.

The 3D classification was performed as already described above, resulting in four distinct 3D class averages (fig. S5): (A) the closed dimer (consisting of two full protomers related by a C2 symmetry), (B) the closed multi-conformer dimer (consisting of one full protomer associated with a second protomer having FATKIN, Pincer, and a flexible Spiral; the two FATKINs in the dimer have C2 symmetry), (C) the open dimer (consisting of one ordered protomer associated with a density corresponding to a second protomer with a conformational change in Pincer), and (D) the open multi-conformer dimer (consisting of a full protomer associated with a second protomer having an ordered FATKIN with Pincer and Spiral not visible). We used statistical movie processing in RELION (*46*) to estimate per-particle beam-induced movement for all 20 movie frames with running averages of 5 movie frames and an SD of 1 pixel for the translational alignments. For each class, we independently used a particle-polishing step (*47*) that fits linear tracks through the estimated particle movement to complete modeling of the beam-induced particle motion. This step included the B-factor weighting to estimate the dose- and resolution-dependent radiation damage with running averages of three movie frames. Below, we describe individual processing of all four 3D classes (fig. S5).

Model building and refinement

We used I-TASSER (*48*) to build an initial homology model of the human ATM FATKIN based on the mTOR FATKIN crystal structure. This model was first rigidly fit to the density for the head in the highest-resolution reconstruction for the closed dimer. We removed all side chains from the model and then used Coot to manually fit the homology model into the density. The model of the N-solenoid was manually built by first fitting a polyalanine model into the largely helical density. An approximate sequence was assigned to this region based on the locations of predicted helices in the sequence. However, no side chains were visible in the density. All atomic models consisting of only backbone atoms and β-carbons (for non-glycine residues)

were refined with PHENIX (phenix_real_space) (*49*). For the refinement, secondary structure elements were restrained. The atomic displacement parameter (ADP) or B-factor refinement was performed in the last macrocycle. The starting model for each of the open conformations was the model of the closed conformation broken into pieces and fit to the density by rigid-body refinement. These models were then manually adjusted using Coot and refined using PHENIX. In the final model for the closed dimer, we have built and refined 4966 of the 6112 residues in the ATM dimer.

Closed dimer (two full protomers visible, 3D class A)

A total of 25,315 polished particles from 3D class A (fig. S5) were auto-refined using the C2 symmetry and a soft spherical mask around the entire volume, which resulted in a final map with an overall resolution of 4.7 Å (rotational and translational alignment accuracies of 1.25° and 0.64 pixel, respectively). The auto-refinement was repeated with a soft mask (5-pixel falloff) around only the Pincer-FATKIN region of the map, excluding the Spiral (the most flexible part of the molecule). This procedure was helpful in obtaining a map of the Pincer-FATKIN region of the closed dimer at a resolution of 4.4 Å (accuracies of 1.65° and 0.65 pixel). This Pincer-FATKIN map was used for initially building the model of this region (see the "Model building and refinement" section). To better resolve the secondary structure elements of the Spiral domain, we carried out focused 3D classification (with fixed particle orientation and a *T* value of 10) of the auto-refined closed dimer particles with the signal from the Pincer-FATKIN subtracted. The auto-refinement (imposed C2 symmetry) of the best 3D class resulted in a map for the Spirals with an overall resolution of 7.9 Å (accuracies of 2.22° and 1.3 pixels). Finally, a model for the Pincer-FATKIN and a model for the Spirals were fitted into the 5.7 Å map that was obtained after the auto-refinement with a soft spherical mask around the entire dimer with no imposed symmetry (accuracies of 1.42° and 0.71 pixel). Plots of the Fourier shell correlation (FSC) between two independently refined half-maps for all four described maps are shown in fig. S6A. The Euler angle distribution for the particles representing a closed dimer is shown in fig. S7A. The schematic overview of the above processing steps is shown in fig. S5.

Closed multi-conformer dimer (only one full protomer visible, 3D class B)

A total of 34,155 polished particles of 3D class B (fig. S5) were auto-refined using no symmetry and a soft solvent mask (5-pixel falloff) around the ordered region of the dimer, which converged to a final map with an overall resolution of 8.8 Å (rotational and translational accuracies of 2.64° and 1.24 pixels). The plot of the FSC between two independently refined half-maps is shown in fig. S6B. The Euler angle distribution for the particles representing the closed multi-conformer dimer is shown in fig. S7B. A focused 3D classification (with the orientation of particles fixed and a *T* value of 10) revealed subclasses with a more apparent density for what resembles a flexible N-solenoid. The schematic overview of these processing steps is shown in fig. S5.

Open dimer (two full protomers visible, 3D class C)

The particles representing 3D class averages of the open dimer, 3D class C (15,837) and the open multi-conformer dimer, 3D class D (44,719) were combined, and auto-refinement was performed using a spherical mask around the entire dimer volume. We have performed seven cycles of the focused classification (without particle realignment, using a *T* value of 10) and 3D refinement (less extensive searches with the initial angular sampling of 3.7° and local searches of 7.5°) to finally obtain the open dimer map from 17,816 particles at a resolution of 11.5 Å (accuracies of 2.3° and 1.28 pixels). The plot of the FSC between two independently refined half-maps is shown in fig. S6C. The Euler angle distribution for the particles representing the open dimer is shown in fig. S7C. The schematic overview of this processing is shown in fig. S5. This dimer has approximately the same dimensions as the closed dimer (Fig. 1), but the relationship of the two molecules to each other is different. One molecule could be readily interpreted by rigidly fitting the ATM protomer into the density. A FATKIN was rigidly fit into the other molecule.

Open multi-conformer dimer (only one full protomer visible, 3D class D)

A total of 44,719 polished particles from 3D class D (fig. S5) were auto-refined with no imposed symmetry and a soft mask (5-pixel falloff) around the ordered region of the dimer, which converged to a map (not shown) with an overall resolution of 7.8 Å (rotational and translational accuracies of 1.76° and 0.83 pixel). A focused 3D classification (*T* value of 10) revealed several good classes containing 19,887 particles altogether. The final auto-refinement converged to a map with an overall resolution of 8.4 Å (accuracies of 2.03° and 0.92 pixel). This map indicated two FATKINs related by approximate C2 symmetry. However, one FATKIN is better ordered than the other. The better-ordered FATKIN has a clearly visible FLAP-BE and a well-defined dimer interface, whereas the other FATKIN does not have a visible FLAP-BE and has a poorly ordered density for its TRD3. The FSC between two independently refined half-maps is plotted in fig. S6D. The Euler angle distribution of the particles representing the open multi-conformer dimer is shown in fig. S7D. A schematic overview of these processing steps is shown in fig. S5.

Open protomer (derived from 3D classes C and D)

The 44,719 particles representing 3D class D, the multi-conformer open dimer (only one full protomer visible), and the 15,837 particles representing 3D class C, the open dimer (two full protomers visible), were combined, and auto-refinement was performed using a soft mask (5-pixel falloff) around the well-ordered protomer. In this way, we obtained a map of the open protomer at an overall resolution of 5.7 Å (accuracies of 1.80° and 0.81 pixel). A further masked auto-refinement around the Pincer-FATKIN region converged to a map with an overall resolution of 4.8 Å (accuracies of 1.79° and 0.82 pixel). Both maps were used to build a complete model of the open ATM protomer (see the "Model building and refinement" section). The plot of the FSC between two independently refined half-maps for both maps is shown in fig. S6E. The Euler angle distribution for the particles representing the open protomer is shown in fig. S7E. The schematic overview of these processing steps is shown in fig. S5. The model of the closed dimer (3D class A) was broken into segments that were fit as rigid bodies into the 4.8 and 5.7 Å resolution densities for the open protomer.

MALS analysis

FLAG-ATM protein for MALS analysis was expressed and purified similarly as described above, except that after elution from the anti-FLAG resin protein, TCEP was added to the eluate to a final concentration of 2 mM. The protein was concentrated in an Ultra-15 Ultracel 100K Concentrator (Millipore, UFC910024) and purified by SEC on a Superose 6 10/300 (GE Healthcare). The entire non-aggregated peak was pooled and concentrated to 1 mg/ml, and 0.1 ml of the sample was further characterized by SEC-MALS using a Wyatt Heleos II 18-angle

light scattering instrument coupled to a Wyatt Optilab rEX online refractive index detector (Wyatt Technology Corporation). Detector 12 in the Heleos instrument was replaced with a WyattQELS detector for dynamic light scattering measurement. The ATM sample was analyzed at room temperature using a Superose 6 10/300 SEC column (GE Healthcare) run at 0.5 ml/min in 25 mM Hepes (pH 7.5, 23°C), 25 mM tris (pH 8.8, 23°C), 150 mM NaCl, 2 mM TCEP, and 0.01% (v/v) Tween 20 buffer before passing through the light scattering and refractive index detectors in a standard SEC-MALS format (fig. S1C). Protein concentration was determined from the excess differential refractive index based on a 0.186 refractive index increment for a protein solution (1 g/ml) or the ultraviolet signal using 1.004 absorbance units/cm for 1 mg/ml. The concentration and the observed scattered intensity at each point in the chromatogram were used to calculate the absolute molecular mass from the intercept of the Debye plot using the Zimm model as implemented in Wyatt's ASTRA software. Autocorrelation analysis of data from the dynamic light scattering detector was also performed using Wyatt's ASTRA software, and the translational diffusion coefficients determined were used to calculate the hydrodynamic radius using the Stokes-Einstein equation and the measured solvent viscosity of 9.3×10^{-3} poise.

SUPPLEMENTARY MATERIALS

Supplementary material for this article is available at http://advances.sciencemag.org/cgi/content/full/3/5/e1700933/DC1

fig. S1. Purification of recombinant human ATM.
fig. S2. Recombinant human ATM is catalytically active.
fig. S3. Cryo-EM images and 2D classes.
fig. S4. Reference models and 3D classes of human ATM.
fig. S5. Summary of the cryo-EM 3D classification and focused refinement of ATM structures.
fig. S6. FSC curves for the observed reconstructions.
fig. S7. Euler angle distribution of particles for each 3D class (A to E).
fig. S8. FSC between the ATM models and EM density maps.
fig. S9. Quality of the density for the highest-resolution human ATM map.
fig. S10. Comparison of the ATM FATKIN with mTOR.
fig. S11. Multiple sequence alignment of the FATKIN regions of human ATM and its representative orthologs, along with that of human mTOR.
fig. S12. Open and closed conformations of the ATM active site.
fig. S13. Domains of the N-solenoid of ATM.
fig. S14. Density bridging the two turns of the Spiral.
fig. S15. Comparison of structurally conserved domains in the N-solenoids of ATM and TOR.
fig. S16. Domain organization of ATM compared with TOR.
fig. S17. Highest-resolution subclass (8.4 Å resolution) of the open multi-conformer dimer (from fig. S5, 3D class D) has one ordered protomer associated with a weakly ordered second FATKIN.
table S1. Data collection and refinement statistics.
table S2. Statistics for refined atomic models.
movie S1. Open and closed conformations of ATM.
References (*51*–*58*)

REFERENCES AND NOTES

1. Y. Shiloh, Y. Ziv, The ATM protein kinase: Regulating the cellular response to genotoxic stress, and more. *Nat. Rev. Mol. Cell. Biol.* **14**, 197–210 (2013).
2. C. J. Bakkenist, M. B. Kastan, DNA damage activates ATM through intermolecular autophosphorylation and dimer dissociation. *Nature* **421**, 499–506 (2003).
3. K. Savitsky, S. Sfez, D. A. Tagle, Y. Ziv, A. Sartiel, F. S. Collins, Y. Shiloh, G. Rotman, The complete sequence of the coding region of the ATM gene reveals similarity to cell cycle regulators in different species. *Hum. Mol. Genet.* **4**, 2025–2032 (1995).
4. T. T. Paull, Mechanisms of ATM activation. *Annu. Rev. Biochem.* **84**, 711–738 (2015).
5. A. Mavrou, G. T. Tsangaris, E. Roma, A. Kolialexi, The ATM gene and ataxia telangiectasia. *Anticancer Res.* **28**, 401–405 (2008).
6. M. B. Kastan, D.-S. Lim, S.-T. Kim, D. Yang, ATM—A key determinant of multiple cellular responses to irradiation. *Acta Oncol.* **40**, 686–688 (2001).
7. Z. Guo, S. Kozlov, M. F. Lavin, M. D. Person, T. T. Paull, ATM activation by oxidative stress. *Science* **330**, 517–521 (2010).
8. G. C. M. Smith, R. B. Cary, N. D. Lakin, B. C. Hann, S.-H. Teo, D. J. Chen, S. P. Jackson, Purification and DNA binding properties of the ataxia-telangiectasia gene product ATM. *Proc. Natl. Acad. Sci. U.S.A.* **96**, 11134–11139 (1999).
9. O. Llorca, A. Rivera-Calzada, J. Grantham, K. R. Willison, Electron microscopy and 3D reconstructions reveal that human ATM kinase uses an arm-like domain to clamp around double-stranded DNA. *Oncogene* **22**, 3867–3874 (2003).
10. J.-H. Lee, T. T. Paull, ATM activation by DNA double-strand breaks through the Mre11-Rad50-Nbs1 complex. *Science* **308**, 551–554 (2005).
11. C. A. Lovejoy, D. Cortez, Common mechanisms of PIKK regulation. *DNA Repair* **8**, 1004–1008 (2009).
12. D. Baretić, R. L. Williams, PIKKs—The solenoid nest where partners and kinases meet. *Curr. Opin. Struct. Biol.* **29**, 134–142 (2014).
13. W. C. Y. Lau, Y. Li, Z. Liu, Y. Gao, Q. Zhang, M. S. Y. Huen, Structure of the human dimeric ATM kinase. *Cell Cycle* **15**, 1117–1124 (2016).
14. M. Sawicka, P. H. Wanrooij, V. C. Darbari, E. Tannous, S. Hailemariam, D. Bose, A. V. Makarova, P. M. Burgers, X. Zhang, The dimeric architecture of checkpoint kinases $Mec1^{ATR}$ and $Tel1^{ATM}$ reveal a common structural organisation. *J. Biol. Chem.* 10.1074/jbc.M115.708263 (2016).
15. X. Wang, H. Chu, M. Lv, Z. Zhang, S. Qiu, H. Liu, X. Shen, W. Wang, G. Cai, Structure of the intact ATM/Tel1 kinase. *Nat. Commun.* **7**, 11655 (2016).
16. H. Yang, D. G. Rudge, J. D. Koos, B. Vaidialingam, H. J. Yang, N. P. Pavletich, mTOR kinase structure, mechanism and regulation. *Nature* **497**, 217–223 (2013).
17. J. J. Seidel, C. M. Anderson, E. H. Blackburn, A novel Tel1/ATM N-terminal motif, TAN, is essential for telomere length maintenance and a DNA damage response. *Mol. Cell. Biol.* **28**, 5736–5746 (2008).
18. N. Fernandes, Y. Sun, S. Chen, P. Paul, R. J. Shaw, L. C. Cantley, B. D. Price, DNA damage-induced association of ATM with its target proteins requires a protein interaction domain in the N terminus of ATM. *J. Biol. Chem.* **280**, 15158–15164 (2005).
19. Z. You, C. Chahwan, J. Bailis, T. Hunter, P. Russell, ATM activation and its recruitment to damaged DNA require binding to the C terminus of Nbs1. *Mol. Cell. Biol.* **25**, 5363–5379 (2005).
20. J.-P. Kruse, W. Gu, Modes of p53 regulation. *Cell* **137**, 609–622 (2009).
21. N. Kanu, T. Zhang, R. A. Burrell, A. Chakraborty, J. Cronshaw, C. DaCosta, E. Grönroos, H. N. Pemberton, E. Anderton, L. Gonzalez, S. Sabbioneda, H. D. Ulrich, C. Swanton, A. Behrens, RAD18, WRNIP1 and ATMIN promote ATM signalling in response to replication stress. *Oncogene* **35**, 4009–4019 (2016).
22. D. Baretić, A. Berndt, Y. Ohashi, C. M. Johnson, R. L. Williams, Tor forms a dimer through an N-terminal helical solenoid with a complex topology. *Nat. Commun.* **7**, 11016 (2016).
23. H. Yang, J. Wang, M. Liu, X. Chen, M. Huang, D. Tan, M.-Q. Dong, C. C. L. Wong, J. Wang, Y. Xu, H.-W. Wang, 4.4 Å resolution cryo-EM structure of human mTOR complex 1. *Protein Cell* **7**, 878–887 (2016).
24. C. H. S. Aylett, E. Sauer, S. Imseng, D. Boehringer, M. N. Hall, N. Ban, T. Maier, Architecture of human mTOR complex 1. *Science* **351**, 48–52 (2016).
25. B. L. Sibanda, D. Y. Chirgadze, D. B. Ascher, T. L. Blundell, DNA-PKcs structure suggests an allosteric mechanism modulating DNA double-strand break repair. *Science* **355**, 520–524 (2017).
26. N. Sandoval, M. Platzer, A. Rosenthal, T. Dörk, R. Bendix, B. Skawran, M. Stuhrmann, R.-D. Wegner, K. Sperling, S. Banin, Y. Shiloh, A. Baumer, U. Bernthaler, H. Sennefelder, M. Brohm, B. H. F. Weber, D. Schindler, Characterization of ATM gene mutations in 66 ataxia telangiectasia families. *Hum. Mol. Genet.* **8**, 69–79 (1999).
27. D. Stoppa-Lyonnet, J. Soulier, A. Laugé, H. Dastot, R. Garand, F. Sigaux, M.-H. Stern, Inactivation of the ATM gene in T-cell prolymphocytic leukemias. *Blood* **91**, 3920–3926 (1998).
28. S. So, A. J. Davis, D. J. Chen, Autophosphorylation at serine 1981 stabilizes ATM at DNA damage sites. *J. Cell Biol.* **187**, 977–990 (2009).
29. D. A. Mordes, G. G. Glick, R. Zhao, D. Cortez, TopBP1 activates ATR through ATRIP and a PIKK regulatory domain. *Genes Dev.* **22**, 1478–1489 (2008).
30. A. Sekulić, C. C. Hudson, J. L. Homme, P. Yin, D. M. Otterness, L. M. Karnitz, R. T. Abraham, A direct linkage between the phosphoinositide 3-kinase-AKT signaling pathway and the mammalian target of rapamycin in mitogen-stimulated and transformed cells. *Cancer Res.* **60**, 3504–3513 (2000).
31. Y. Sun, X. Jiang, S. Chen, N. Fernandes, B. D. Price, A role for the Tip60 histone acetyltransferase in the acetylation and activation of ATM. *Proc. Natl. Acad. Sci. U.S.A.* **102**, 13182–13187 (2005).
32. Y. Sun, Y. Xu, K. Roy, B. D. Price, DNA damage-induced acetylation of lysine 3016 of ATM activates ATM kinase activity. *Mol. Cell. Biol.* **27**, 8502–8509 (2007).
33. W. M. Abbott, B. Middleton, F. Kartberg, J. Claesson, R. Roth, D. Fisher, Optimisation of a simple method to transiently transfect a CHO cell line in high-throughput and at large scale. *Protein Expr. Purif.* **116**, 113–119 (2015).

34. O. Daramola, J. Stevenson, G. Dean, D. Hatton, G. Pettman, W. Holmes, R. Field, A high-yielding CHO transient system: Coexpression of genes encoding EBNA-1 and GS enhances transient protein expression. *Biotechnol. Prog.* **30**, 132–141 (2014).
35. A. C. Joerger, M. D. Allen, A. R. Fersht, Crystal structure of a superstable mutant of human p53 core domain. Insights into the mechanism of rescuing oncogenic mutations. *J. Biol. Chem.* **279**, 1291–1296 (2004).
36. P. V. Nikolova, J. Henckel, D. P. Lane, A. R. Fersht, Semirational design of active tumor suppressor p53 DNA binding domain with enhanced stability. *Proc. Natl. Acad. Sci. U.S.A.* **95**, 14675–14680 (1998).
37. M. Bista, S. M. Freund, A. R. Fersht, Domain-domain interactions in full-length p53 and a specific DNA complex probed by methyl NMR spectroscopy. *Proc. Natl. Acad. Sci. U.S.A.* **109**, 15752–15756 (2012).
38. R. L. Weinberg, D. B. Veprintsev, A. R. Fersht, Cooperative binding of tetrameric p53 to DNA. *J. Mol. Biol.* **341**, 1145–1159 (2004).
39. X. Li, S. Zheng, D. A. Agard, Y. Cheng, Asynchronous data acquisition and on-the-fly analysis of dose fractionated cryoEM images by UCSFImage. *J. Struct. Biol.* **192**, 174–178 (2015).
40. X. Li, P. Mooney, S. Zheng, C. R. Booth, M. B. Braunfeld, S. Gubbens, D. A. Agard, Y. Cheng, Electron counting and beam-induced motion correction enable near-atomic-resolution single-particle cryo-EM. *Nat. Methods* **10**, 584–590 (2013).
41. K. Zhang, Gctf: Real-time CTF determination and correction. *J. Struct. Biol.* **193**, 1–12 (2016).
42. S. H. W. Scheres, RELION: Implementation of a Bayesian approach to cryo-EM structure determination. *J. Struct. Biol.* **180**, 519–530 (2012).
43. S. H. W. Scheres, A Bayesian view on cryo-EM structure determination. *J. Mol. Biol.* **415**, 406–418 (2012).
44. S. H. W. Scheres, Semi-automated selection of cryo-EM particles in RELION-1.3. *J. Struct. Biol.* **189**, 114–122 (2015).
45. G. Tang, L. Peng, P. R. Baldwin, D. S. Mann, W. Jiang, I. Rees, S. J. Ludtke, EMAN2: An extensible image processing suite for electron microscopy. *J. Struct. Biol.* **157**, 38–46 (2007).
46. X.-C. Bai, I. S. Fernández, G. McMullan, S. H. W. Scheres, Ribosome structures to near-atomic resolution from thirty thousand cryo-EM particles. *eLife* **2**, e00461 (2013).
47. S. H. W. Scheres, Beam-induced motion correction for sub-megadalton cryo-EM particles. *eLife* **3**, e03665 (2014).
48. J. Yang, R. Yan, A. Roy, D. Xu, J. Poisson, Y. Zhang, The I-TASSER Suite: Protein structure and function prediction. *Nat. Methods* **12**, 7–8 (2015).
49. P. Zwart, P. V. Afonine, R. W. Grosse-Kunstleve, L.-W. Hung, T. R. Ioerger, A. J. McCoy, E. McKee, N. W. Moriarty, R. J. Read, J. C. Sacchettini, N. K. Sauter, L. C. Storoni, T. C. Terwilliger, P. D. Adams, Automated structure solution with the PHENIX suite. *Methods Mol. Biol.* **426**, 419–435 (2008).
50. Z. Q. Bao, D. M. Jacobsen, M. A. Young, Briefly bound to activate: Transient binding of a second catalytic magnesium activates the structure and dynamics of CDK2 kinase for catalysis. *Structure* **19**, 675–690 (2011).
51. I. Hickson, Y. Zhao, C. J. Richardson, S. J. Green, N. M. B. Martin, A. I. Orr, P. M. Reaper, S. P. Jackson, N. J. Curtin, G. C. M. Smith, Identification and characterization of a novel and specific inhibitor of the ataxia-telangiectasia mutated kinase ATM. *Cancer Res.* **64**, 9152–9159 (2004).
52. A. Kucukelbir, F. J. Sigworth, H. D. Tagare, Quantifying the local resolution of cryo-EM density maps. *Nat. Methods* **11**, 63–65 (2014).
53. E. F. Pettersen, T. D. Goddard, C. C. Huang, G. S. Couch, D. M. Greenblatt, E. C. Meng, T. E. Ferrin, UCSF Chimera—A visualization system for exploratory research and analysis. *J. Comput. Chem.* **25**, 1605–1612 (2004).
54. Y. Liu, B. Schmidt, D. L. Maskell, MSAProbs: Multiple sequence alignment based on pair hidden Markov models and partition function posterior probabilities. *Bioinformatics* **26**, 1958–1964 (2010).
55. R. D. Finn, J. Clements, S. R. Eddy, HMMER web server: Interactive sequence similarity searching. *Nucleic Acids Res.* **39**, W29–W37 (2011).
56. W. Kabsch, C. Sander, Dictionary of protein secondary structure: Pattern recognition of hydrogen-bonded and geometrical features. *Biopolymers* **22**, 2577–2637 (1983).
57. A. Drozdetskiy, C. Cole, J. Procter, G. J. Barton, JPred4: A protein secondary structure prediction server. *Nucleic Acids Res.* **43**, W389–W394 (2015).
58. X. Robert, P. Gouet, Deciphering key features in protein structures with the new ENDscript server. *Nucleic Acids Res.* **42**, W320–W324 (2014).

Acknowledgments: We thank O. Perisic for help in expressing and purifying ATM and for comments on the manuscript. We thank A. Berndt for help with cryo-EM data collection and for comments on the manuscript and F. Begum, S. Maslen, M. Skehel, and S.-Y. Peak-Chew for help with mass spectrometry. We are grateful to S. Scheres for the advice and comments on the manuscript. We thank X.-C. Bai for advice with cryo-EM data processing, S. Chen and C. Savva for help with the data collection, and J. Grimmett and T. Darling for assistance with the LMB computing cluster. We thank K. Sader of the Cambridge Pharmaceutical CryoEM Consortium and R. Matadeen of FEI for help with data collection. **Funding:** This work was funded by the MRC (MC_U105184308 to R.L.W.) and the AstraZeneca/LMB Blue Skies Initiative (MC_A024-5PF9H R.L.W. and C.P.). **Author contributions:** D.B. designed and performed most experiments (purified protein and prepared cryo-EM grids, collected and processed EM data, and carried out kinase assays). D.B., R.L.W., and C.P. carried out data analysis. C.M.J. performed MALS experiments and analysis. H.K.P. and C.M.T. developed purification protocols. D.I.F. and D.B. expressed protein. B.S. made the sequence alignment. T.K. expressed and purified p53. A.R.F. provided reagents and advice for work with p53. D.B. and R.L.W. carried out model building and wrote the manuscript. C.P. and R.L.W. organized the collaboration. **Competing interests:** The authors declare that they have no competing interests. **Data and materials availability:** All data needed to evaluate the conclusions in the paper are present in the paper and/or the Supplementary Materials. Additional data related to this paper may be requested from the authors. Coordinates (closed dimer PDB ID 5NP0 and open protomer PDB ID 5NP1) and densities [closed dimer (C2) EMD-3668, closed dimer (C1) EMD-3669, closed dimer Pincer-FATKIN EMD-3670, open dimer EMD-3671, open protomer EMD-3672, and open protomer Pincer-FATKIN EMD-3673] are deposited with the wwPDB OneDep System.

Submitted 20 March 2017
Accepted 19 April 2017
Published 10 May 2017
10.1126/sciadv.1700933

Citation: D. Baretić, H. K. Pollard, D. I. Fisher, C. M. Johnson, B. Santhanam, C. M. Truman, T. Kouba, A. R. Fersht, C. Phillips, R. L. Williams, Structures of closed and open conformations of dimeric human ATM. *Sci. Adv.* **3**, e1700933 (2017).